Short summary. 250 m estimates of snow water equivalent in the Western US and Canada are improved by assimilating observations representative of a snow-focused satellite mission with a land surface model. Here, by including a gap-filling strategy, snow estimates could be improved in forested regions where remote sensing is challenging. This approach improved estimates of winter maximum snow water volume to within 4%, on average, with persistent improvements to both spring snow and runoff in many regions.

Extending the utility of space-borne snow water equivalent observations over vegetated areas with data assimilation

Justin M. Pflug[1,2], Melissa L. Wrzesien[1,2], Sujay V. Kumar[2], Eunsang Cho[1,2,a], Kristi R. Arsenault[3,2], Paul R. Houser[4], Carrie M. Vuyovich[2]

[1]Earth System Science Interdisciplinary Center, University of Maryland, College Park, MD, USA
[2]Hydrological Sciences Laboratory, NASA Goddard Space Flight Center, Greenbelt, MD, USA
[3]Science Applications International Corporation, McLean, VA, USA
[4]Geography and Geoinformation Science Department, George Mason University, Fairfax,VA, USA
[a]current address: Ingram School of Engineering, Texas State University, San Marcos, TX, USA

Correspondence to: Justin Pflug (Justin.Pflug@nasa.gov)

> **Formatted:** Space Before: 0 pt

Abstract. Snow is a vital component of the Earth system. Yet, no snow-focused satellite remote sensing platform currently exists. In this study, we investigate how synthetic observations of snow water equivalent (SWE) representative of a synthetic aperture radar remote sensing platform could improve spatiotemporal estimates of snowpack. We use a fraternal twin Observing System Simulation Experiment, specifically investigating how much snow simulated using widely used models and forcing data could be improved by assimilating synthetic observations of SWE. We focus this study across a 24°-by-37° domain in the Western United States (US) and Canada, simulating snow at 250 m resolution and hourly timesteps in water-year 2019. We perform two data assimilation experiments, including: 1) a simulation excluding synthetic observations in forests where canopies obstruct remote sensing retrievals, and 2) a simulation inferring snow distribution in forested grid cells using synthetic observations from nearby canopy-free grid cells. Results found that, relative to a nature run, or assumed true simulation of snow evolution, assimilating synthetic SWE observations improved average SWE biases at maximum snowpack timing in shrub, grass, crop, bare-ground, and wetland land cover types from 14%, to within 1%. However, forested grid cells contained a disproportionate amount of SWE volume. In forests, SWE mean absolute errors at the time of maximum snow volume were 111 mm, and average SWE biases were on the order of 150%. Here, the data assimilation approach that estimated forest SWE using observations from the nearest canopy-free grid cells substantially improved these SWE biases (18%) and the SWE mean absolute error (27 mm). Simulations employing data assimilation also improved estimates of the temporal evolution of both SWE and runoff, even in spring snowmelt periods when melting snow and high snow liquid water content prevented synthetic SWE retrievals. In fact, in the Upper Colorado River region, melt-season SWE biases were improved from 63% to within 1%, and the Nash Sutcliffe Efficiency of runoff improved from –2.59 to 0.22. These results demonstrate the

34   value of data assimilation and a snow-focused globally relevant remote sensing platform for improving the characterization of

35   SWE and associated water availability.

1 Introduction

37   Snow plays important roles in the Earth system by regulating global temperatures and cooling the land surface because of

38   its reflective properties (Barry, 2002). Snow is also a major source of water storage for many regions, especially in areas that

39   rely on snowpack to sustain water resources during the dry season. In fact, it has been estimated that more than 2 billion people

40   around the world are reliant on seasonal snow melt for their water supply (Barnett et al., 2005). Snowpack is the natural

41   'integrator' of climatic conditions and offers more predictability of water availability than variables with shorter memory, such

42   as precipitation and streamflow (Terzago et al., 2023). Accurate wintertime estimates of snowpack are therefore critical for

43   water management and agricultural planning (Koster et al., 2010). For example, in the Western US, where a vast majority of

44   streamflow originates from snow (Li et al., 2017), it is common practice to use the April 1 snowpack, the historic date of

45   maximum snowpack in that region, for developing water supply estimates for later in the season. However, climate change

46   impacts have led to increased variability in the snow seasonality (Livneh and Badger, 2020), with warmer temperatures

47   reducing the amount of snow accumulation and seasonal snow storage, and advancing the timing of the spring melt. Therefore,

48   accurate characterization of winter snowpack and its variability is critically important for making informed water supply

49   quantifications.

50   In recognition of the critical need to have spatially distributed measurements of snow mass, there have been several efforts

51   to measure and estimate SWEfrom many different remote sensing platforms in the past several decades. Airborne lidar systems

52   have been able to provide high resolution, accurate measurements of snow mass (Painter et al., 2016), but this approach has

53   significant logistical barriers for global and frequent snow measurements, and the hydrological utility of a practical spaceborne

54   lidar platform is limited (Kwon et al., 2021). In the past three decades, snow depth and SWE estimates have been derived from

55   passive microwave remote sensing measurements, but these measurements are at coarse spatial resolutions, and have limited

56   accuracies over deep and wet snow, complex terrain, and dense vegetation (Derksen et al., 2014; Foster et al., 2005). Active

57   microwave remote sensing instruments such as Synthetic Aperture Radars (SARs) can provide finer spatial resolution

58   measurements to help resolve some of these issues. For example, C-band SAR observations from the Sentinel-1 constellation

59   have shown promise in obtaining high quality, moderate resolution (1km) observations in deep snow environments (Lievens

60   et al., 2019). A volume scattering radar approach, using X- and Ku-band SAR, has also been demonstrated in several airborne

61   campaigns and proposed for multiple snow mission concepts (Yueh et al 2009, Rott et al 2010) because of its potential to

62   achieve high resolution and global coverage over a range of snow depths. While these microwave instruments can observe in

63   night-time and cloudy conditions, they are still limited over areas with dense vegetation (Tsang et al., 2022). Further, all

64   spaceborne instruments have inherent coverage gaps due to their orbital and revisit configurations.

To overcome these limitations, modeling and data assimilation systems are needed that can extend the coverage and utility of available measurements to areas, times, and variables that are not directly observed. In this article, we present a novel approach through data assimilation, designed specifically to improve the usefulness of spaceborne SWE retrievals over forested areas. The approach is demonstrated using an observing system simulation experiment (OSSE; e.g., Cho et al., 2023; Errico et al., 2007) which is an approach used to formally assess the impact of the data to be collected from an anticipated mission. Several prior studies have examined the use of OSSEs for snow mission studies (Garnaud et al., 2019; Kwon et al., 2021; Wrzesien et al., 2022). Among them, SAR-focused OSSEs have been conducted by Garnaud et al. (2019) and Cho et al. (2023) to assess the utility of hypothetical snow observations. Garnaud et al. (2019) focused on a Ku-band SAR to quantify trade-offs between sensor configurations (e.g., various spatial resolutions and revisit frequencies) with retrieval algorithm accuracy and SWE performance in southern Quebec, Canada, where temperate forests are dominant with shallow and moderate snowpack conditions. Cho et al. (2023) conducted a X-/Ku-band SAR OSSE with an achievable sensor configuration (1 km spatial resolution, 7-day revisit frequency, and orbital configurations) focusing on mountainous environments in a western Colorado and testing the degree to which various SAR retrieval capabilities in different forest densities and snow volumes could improve observationally-based SWE estimates. Here, we build on this prior research by developing an OSSE covering the entire western US and portions of Canada. We simulate finer-scale (250 m) synthetic SWE observations that could be provided from a future X-/Ku-band SAR mission, which are then incorporated within a land surface model through data assimilation to assess their capability to improve snow state estimates, and the integrated impact on hydrologic states in space and time. The assimilation experiments here are conducted with and without a novel strategy to extend SAR-based SWE estimates from unforested regions into forested landscapes where SAR retrievals of the snowpack may be obscured by the forest canopy.

The primary contribution of this paper is the development of a viable strategy for extending hypothetical remotely sensed SWE retrievals from a volume-scattering X-/Ku-band SAR satellite mission into difficult-to-observe forest landscapes. We specifically focus on addressing the following research questions: 1) what is the added utility of spaceborne active remote sensing SWE retrievals (assuming retrievals meet currently defined mission requirements) across the Western US and Canada? 2) how much can spatiotemporal representations of SWE be improved by focusing on developing observationally based snow estimates over areas with dense vegetation, where SAR sensors may be limited? 3) How much added hydrological utility can be obtained through spaceborne active remote sensing measurements and data assimilation approaches, particularly when coverage over forested areas is improved?

Section 2 describes the study domain and OSSE modeling setup. This is followed by the description of the results (Sect. 3), a discussion of the findings (Sect. 4), and the study's conclusions (Sect. 5).

2.1 Study domain and OSSE setup

An OSSE is used to assess the value of the data to be collected from an anticipated mission. OSSEs often consist of the following steps: 1) Developing a "nature run" that uses a state-of-the-art model employed with the best available boundary conditions (Sect. 2.1); 2) using the nature run to generate simulated remote sensing observations, accounting for sources of sensing limitations, sensing uncertainties, and orbital configurations (Sect. 2.2); 3) incorporating the simulated observations (often through data assimilation, Sect. 2.3) in a separate, "open loop" model configuration with accuracies representative of common modeling biases and uncertainties; and 4) evaluating how much the simulated remote sensing data improve the open loop model performance relative to the nature run. In addition to this OSSE approach, this study goes further by 1) testing the degree of improvement to both the remotely-sensed variable (i.e., SWE) and the resulting changes to land surface runoff in snowy covered regions, and 2) developing two separate data assimilation experiments, one which masks simulated observations in forested pixels where SAR retrievals may be most challenging, and the other including a novel approach for inferring SWE in forested pixels using simulated observations from nearby, unforested pixels (Sect. 2.4). The details of the OSSE setup used in this study are described in more depth throughout this section.

We employ the NASA Land Information System (LIS; Kumar et al., 2006), an infrastructure for high performance, ensemble-based land surface modelling and data assimilation to enable this OSSE. LIS encompasses several advanced land surface models that can simulate terrestrial water, energy, and carbon balances and related states such as soil moisture, land surface temperature, and SWE, among others. These include different versions of community models such as Noah (Ek et al., 2003), Variable Infiltration Capacity (VIC; Liang et al., 1994), Catchment (Koster et al., 2000), Joint UK Land Environment Simulator (JULES; Best et al., 2011), and Noah-MP (Niu et al., 2011). The LIS framework also includes support for specialized models that are designed to provide more detailed representations of certain land surface processes (e.g. snow), while enabling interaction with LSMs that solve for water, energy, and carbon balances at a macroscale. For example, the advanced snow physics model called SnowModel (Liston and Elder, 2006) has been incorporated within LIS in a manner that allows coupling to existing LSMs. This structure allows the use of the advanced snow physics from SnowModel while leveraging the existing process schemes (e.g., sub-surface, groundwater, canopy) within the LSMs. Here we utilize these unique capabilities for enabling the OSSE integrations. . The study is conducted over a large domain (Fig. 1), covering the Western US and southern Canada from 31-55N and 93-130W at a 250 m spatial resolution. As shown in Fig. 1, this modeling domain encompasses a broad range of vegetation types, topographical regimes and water resources regions of the Pacific Northwest, California, Great Basin, and Upper Colorado. 22% of the domain is covered by forests, with grasslands, croplands, and shrublands accounting for 20%, 23%, and 26% of the domain, respectively. Forests dominate the coverage of areas with significant snowpack, occupying 58% of regions that are in the mid-elevation range of 2500-3500m, and 15% of the areas with elevations over 3500m. From a modeling perspective, the domain extent of Fig. 1 (~83 million land grid points) is computationally challenging. The scalable high performance computational and parallel inputting and outputting capabilities of NASA LIS were leveraged to enable these simulations. A multiprocessor configuration involving approximately 1000 processors was employed to facilitate large model simulations for the nature run, open loop simulation, and two simulations with data assimilation.
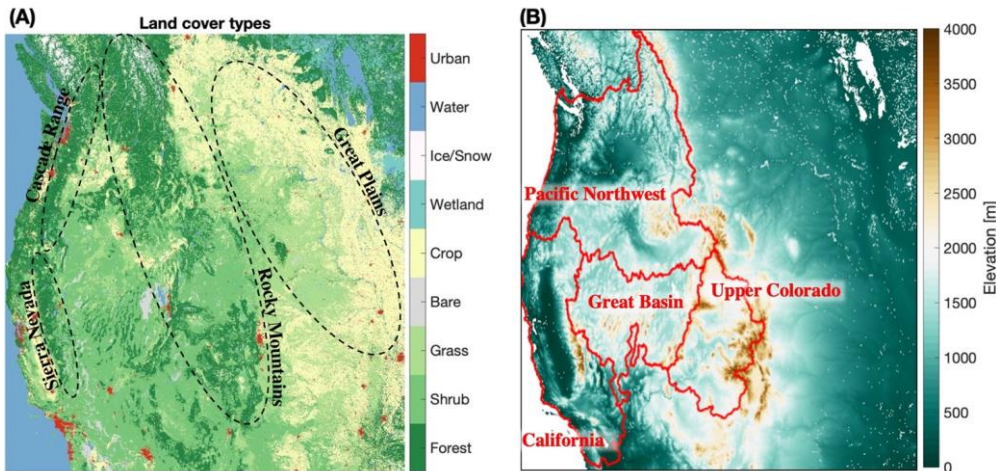
128
129 **Figure 1:** Maps of the land and vegetation classes (A; left panel) and elevation (in meters) (B; right panel) used in the
130 simulations. Outlines and labels in the left panel indicate regions discussed in the Results (Sect. 4). Red contours in the right
131 panel indicate hydrologic regions used in the analysis.

132 Simulations in this study are conducted by forcing LIS LSMs with the surface meteorology from NASA's Modern Era

133 Retrospective Reanalysis, version 2 (MERRA-2; Gelaro et al., 2017) and ECMWF Reanalysis, version 5 (ERA5; Hersbach et

134 al., 2020) products. The model integrations were conducted for the water year 2019 (September 2018 – September 2019),

135 which was a wetter than normal year based on the long-term average meteorological conditions over this domain.

136 The open loop and data assimilation integrations performed in this study are conducted using the Noah land surface model

137 with multi-parameterization (Noah-MP) version 4.0.1 (Niu et al., 2011) and forcing from ERA5.The Noah-MP model evolved

138 from the Noah LSM, with multiple options for various land surface processes. It represents energy, water, and carbon balances

139 at the land surface by accounting for processes related to infiltration, evaporation, transpiration, runoff generation and

140 groundwater recharge. A TOPMODEL-based runoff model (Beven et al., 2021) is used to calculate surface runoff and

141 groundwater discharge. Options for prognostic vegetation dynamics models that represent the growth and senescence of

142 vegetation are also available within Noah-MP. A two-stream radiative transfer approach is employed to calculate surface

143 energy processes. Finally, a multilayer snowpack model (with up to three layers) is used to account for snow melt

144 metamorphisms, compaction by overlying snow, sublimation of canopy intercepted snow, and snowmelt-refreeze cycles within

145 Noah-MP (Niu and Yang, 2004).

146 Snow states like snow depth and SWE were also modeled across the Western US (domain highlighted in Fig. 1) at 250 m

147 resolution and hourly time steps using a state-of-the-art and physically based single-layer snow model(named SnowModel;

148   Liston and Elder, 2006), provided forcing from MERRA-2 with LIS-provided lapse rates and topography-based meteorological

149   downscaling approaches, like incoming shortwave corrections based on topographical shading (Cosgrove et al., 2003; Kumar

150   et al., 2013). SnowModel has seen widespread use in the snow community, demonstrating the capability to resolve snow

151   evolution in a variety of landscapes and complex snow processes like the redistribution of snow via wind, and the resulting

152   impact on snow distribution, melt season snow duration, glacier mass balance, and snow habitat for species like polar bears

153   and Dall sheep (Hiemstra et al., 2002; Liston et al., 2016; Mahoney et al., 2018; Mernild et al., 2017; Sturm and Wagner,

154   2010). In addition to wind redistribution, snow evolution within SnowModel accounts for a wide set of snow processes,

155   including snow sublimation, snow grain size evolution, solar topographical shading, canopy shading, and canopy snow

156   interception. Through the coupling within LIS, Noah-MP snow states and the resulting snow-driven runoff were updated using

157   the SnowModel outputs at hourly timesteps for each grid cell.

158   Preliminary research has shown that relative to Noah-MP, LIS simulations coupling Noah-MP with SnowModel have

159   improved the volume and spatial distribution of simulated snow depth and SWE (Arsenault et al., 2021; Wrzesien et al., 2022).

160   Therefore, the coupled SnowModel and Noah-MP model was a prime candidate for the "nature run" in this study, or the

161   simulation most representative of the true underlying spatiotemporal snow states from which simulated observations were

162   derived (Sect. 2.2), and the assimilated model was compared against. Here, the nature run and open loop simulations detailed

163   above were compared to a widely-used Western US snow reanalysis product (Fang et al., 2022) to ensure that 1) the nature

164   run exhibited reasonable model accuracy, and 2) the departure between the open loop simulation and nature run are

165   representative of common regional, continental, and global modeling efforts (Figure S1 and S2). The OSSE developed for this

166   study is a "fraternal twin" OSSE, wherein two different models are used to simulate snow in the open loop (Noah-MP) and

167   nature run (SnowModel) simulations. This approach is selected since "identical twin" OSSEs, which use the same model, can

168   result in less divergence in model states and information content, biasing the degree of model improvement that could come

169   from assimilating an observation (e.g., Yu et al., 2019). More information on the difference between the open loop and nature

170   run models can be found in Table S1.

171   **2.2 Observation simulator**

172   . Synthetic SWE retrievals at 250 m spatial resolution, representative of a hypothetical X- and Ku-band SAR mission, are

173   simulated from the nature run. To do this, the orbital swaths are simulated using TAT-C (Le Moigne et al., 2017). TAT-C is a

174   NASA software system designed for future Distribution Spacecraft Missions (DSM), which enables us to explore a range of

175   feasible design options (e.g., constellation vs. single, geostationary vs. polar-orbiting, low vs. high temporal frequencies) to

176   estimate optimal gains for the given mission configuration. Previous OSSEs have been conducted to test the impact from

177   different snow mission configurations (e.g. Garnaud et al 2019). Here we instead focus on demonstrating the value of a gap-

178   filling approach (Sect. 2.4) for estimating snow in forested landscapes where SAR retrievals may be most challenging.

179   Therefore, we used TAT-C to design a conservative mission configuration consisting of a small constellation of X- and Ku-

180 band SAR satellites. Using a 10-14 day revisit frequency, depending on latitude, TAT-C orbital swaths were applied to the

181 nature run outputs to simulate the satellite viewing area. The remote sensing spatial coverage is simulated by extending the

182 ground track to a swath width. The daily viewing extents are then simulated as a daily binary map (so-called "cookie cutter")

183 masking the surface as viewed or not at a 250 m spatial resolution.

184 Based on an error level of 20%, spatially and temporally uncorrelated random errors drawn from a Gaussian distribution are

185 added to the synthetic SWE retrievals. This 20% error level is selected using a conservative estimate of SWE measurement

186 uncertainty for a volume-scattering X-/Ku -band SAR mission based on developed mission design concepts and ground

187 validation. For example, the ESA Cold Regions Hydrology High-Resolution Observatory (CoREH2O) mission expected to

188 meet instrument and retrieval requirements of ± 30 mm accuracies for SWE of 300 mm, $\pm 10\%$ for SWE greater than 300 mm

189 (Rott et al 2010, 2012). Similarly, the Canadian Terrestrial Snow Mass Mission (TSMM) concept that is currently under

190 development aims to achieve better than 20% measurement uncertainty for SWE greater than 50 mm, though it is expected to

191 have higher uncertainties in deep snow conditions (e.g., $\geq$ 200 mm SWE)limited to SWE less than 200 mm due to the dual

192 Ku-band system (Garnaud et al. 2019). Airborne and tower-based field data have demonstrated that a combination X- and Ku-

193 band system can provide SWE retrievals over a range of snow conditions at accuracies better than 20% (Zhu et al. 2018, 2021,

194 Tsang et al 2022, Durand et al. 2023, Singh et al. 2023). However, we use an assumption of uniform error levels throughout

195 the domain, whereas in reality, the errors are likely to be dependent on other factors, including the terrain characteristics, snow

196 characteristics, and vegetation. This is discussed more in Section 4.

197 **2.3 Data assimilation setup**

198 A one-dimensional ensemble Kalman Filter (EnKF; Reichle et al., 2002) is used to assimilate the synthetic observations

199 within the open loop configuration of the model. EnKF is widely used for land data assimilation studies (Kumar et al., 2022),

200 as it provides a flexible approach for the treatment of model and observation errors and non-linear models. An ensemble of

201 model realizations is used by EnKF to assess and propagate model errors. In this instance, the ensemble requirement further

202 adds to the significant computational requirements of the large model domain (Fig. 1) and fine spatial resolution of the

203 simulations (250 m). Therefore, a 5-member ensemble with perturbations applied to the meteorological variables and model

204 prognostic fields are used for simulating uncertainty in the modeled estimates. Table 1 details the parameters for meteorological

205 and model state perturbations, which are based on recent snow data assimilation studies (Lahmers et al., 2022; Kwon et al.,

206 2021). Though a larger ensemble size is better for ensuring sufficient sampling density, our choice of five ensembles is

207 reasonable given that the model state vector used in the assimilation only consists of two variables; the total SWE and snow

208 depth. The assimilation setup employs a sequential update strategy, where at each time step an ensemble of model forecasts is

209 propagated forward in time, followed by an update based on observational inputs. The model states are updated toward the

210 observations based on the relative uncertainties in the model and observations using the following formulation, at a certain

211 time k.

212
$$x_k^{i+} = x_k^{i-} + K_k\left[y_k^i - H_k x_k^{i-}\right] \qquad \text{Eq. (1)}$$

213 Where x_k and y_k are the model and observation state vectors, respectively. The term H_k represents the observation operator
214 that maps the model states to the observed variables. The superscripts $i-$ and $i+$ represent the ith ensemble member before
215 and after the update, respectively. K_k is the "Kalman gain" term, that allows the weighting of the observations and model
216 forecasts is a function of the model and observation error covariances.

217 **Table 1.** Model forcing and state-variable perturbations used by the 5-member ensemble of LIS simulations

Variable	Perturbation Type	Std. Dev.	Cross Correlation across variables			
Meteorological Forcing			SW corr	LW corr	PCP corr	T corr
Downward Shortwave (SW)	Multiplicative	0.2	1	−0.3	−0.5	0.3
Downward Longwave (LW)	Additive	30	−0.3	1	0.5	0.6
Precipitation (PCP)	Multiplicative	0.5	−0.5	0.5	1	−0.1
Near surface Air Temperature (T)	Additive	0.5	0.3	0.6	−0.1	1
Noah-MP LSM snow states			SWE	Snow depth		
SWE	Multiplicative	0.01	1	0.9		
Snow depth	Multiplicative	0.01	0.9	1		

218
219   The data assimilation procedure detailed here assimilated the synthetic SWE retrievals (Sect. 2.2) with the open loop
220 simulation. The degree to which the simulation with data assimilation approached SWE simulated by the nature run is intended
221 to represent the extent to which a SAR remote sensing platform with the SWE retrieval characteristics from Sect. 2.2 could be
222 combined with a land surface model to provide near real-time estimates of SWE at 250 m resolution. However, the SAR
223 observations synthesized in this study have known issues with observing snow with high liquid water contents and dense forest
224 cover. Therefore, synthetic observations at each timestep were masked at grid cells where the most-dominant landcover type
225 from the North American Land Change Monitoring System (NALCMS; Latifovic et al., 2017) was forested, including
226 deciduous, evergreen, and mixed forest cover (Fig. 1). Synthetic observations were also masked at grid cells where and when

227   snow was experiencing melt, identified by the presence of liquid water in the snowpack from the nature run. Although limited

228   in area, grid cells with "ice" landcover (Fig. 1) were also excluded. In this study, this simulation which used assimilation only

229   in unforested, non-melting, and ice-free grid cells is termed "Data Assimilation, without the forest strategy" (DA). In Sect. 2.4

230   below, we present a novel approach used to infer SWE in grid cells with forests using the nearest canopy-free synthetic

231   observations.

2.4 Extending observations over forests

233   The 1-d EnKF approach employed here updated each model grid SWE from the open loop simulation based on the

234   observations available at that grid point. Though studies have employed 3-d EnKF approaches to spatially propagate

235   observational information to neighbouring grid cells (De Lannoy et al., 2012), here we relied on 1-d updates due to several

236   factors. First, a 2-d update requires the knowledge of spatial error correlations and their variability, which is challenging to

237   specify (Ying, 2020). Most prior studies using such schemes employ uniform specifications and are limited to small domains.

238   Second, a 2-d update increases the size of the state vector and consequently requires the use of a larger ensemble. This,

239   combined with the added computational expense of a 2-d analysis significantly increases the computational cost. Therefore,

240   we employed an alternate approach that is computationally more efficient while allowing the extension of observations to

241   nearby areas.

242   Assuming that the SWE retrievals from the hypothetical SAR instrument are limited over areas where the dominant

243   vegetation type are forests (Fig. 1a), we employ a novel approach to extend the observations obtained in non-forested areas

244   (Fig 2). For every forested location, valid retrievals over nearby non-forested locations within a radius of influence of 750 m

245   are identified. An observation at the forested pixel is then estimated by scaling the model SWE by the ratio of the average

246   observed SWE to modeled SWE over the 'clearing' areas (Fig. 2). This scaled observation is then used for assimilation over

247   the forested pixel. Here we implicitly use the spatial correlations inherent in the model between forested and clearing areas to

248   extend observational coverage over the clearing to forested locations. This simulation is termed "Data Assimilation, with the

249   forest strategy" (symbolized by DA+F in Section 3). To evaluate the accuracy and added value of this scaling approach, we

250   compare SWE and runoff from the nature run simulation, versus simulations with data assimilation both 1) employing the

251   forest scaling strategy discussed here, and 2) masking synthetic observations in forested grid cells (Sect. 2.3).

252

253
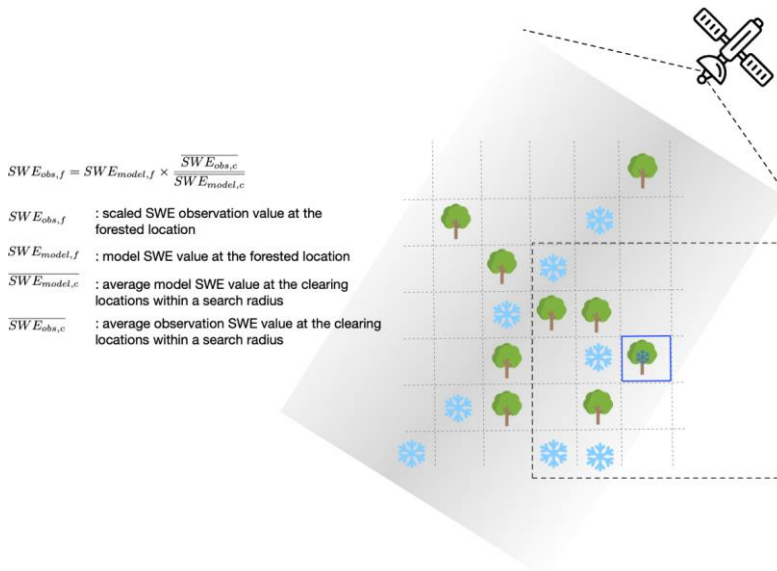
Figure 2. Conceptual depiction and equations demonstrating the forest strategy used here, which estimates a SWE observation at a given grid cell (outlined box in blue color) based on the modeled SWE ($SWE_{model,f}$) and the ratio between the average synthetic SWE observations ($\overline{SWE_{obs,c}}$) and average modeled SWE ($\overline{SWE_{model,c}}$) from grid cells within a 750 m radius (dashed box). The light gray shading represents the satellite swath, the tree icons indicate forested locations, and the snowflake icons represent grid cells with valid SWE retrievals at non-forested locations. The grid cell from this example is near the satellite swath edge, so observations are unavailable in the nearby regions South and East of this pixel.

3 Results

In this section, we compute the difference between the open loop simulation, nature run, and the two open loop simulations with data assimilation, one masking synthetic observations over regions with forests, and time periods with melting snow, and ice, and the other applying the same data assimilation but extending snow estimates in forested regions using the strategy from Sect. 2.4 and Fig. 2. The differences between these simulations are detailed in Section 2 and Table S1. We focus on the differences between these four simulations using: 1) average SWE from the winter snow accumulation season (December, January, and February; DJF), when snowmelt is minimized and synthetic observations are masked by grid cells with liquid water content to the smallest degree, 2) spatially distributed SWE on 13 March, the date corresponding to the timing of maximum SWE volume in water-year 2019, and 3) daily average SWE and total runoff for each day in water-year 2019 over a number of selected hydrologic regions including the Pacific Northwest, California, Great Basin, and Upper Colorado (Fig. 1b).

271   The open loop and nature run simulations exhibited differences in both the volume and spatial distribution of average winter
272   (December, January, and February; DJF) SWE (Fig. 3a and 3b). Relative to the nature run, the open loop simulation tended to
273   simulate lower elevation winter SWE that was both larger in magnitude and persisted for longer before melting. In the Pacific
274   Northwest domain (Fig. 4), DJF average snow cover (defined as grid cells with mean DJF SWE exceeding 5 mm), was
275   approximately 12% larger for the open loop simulation than the nature run (Table 2). These snow extent biases were also
276   apparent in the other hydrologic regions (Figs. S3 – S5), where open loop snow extents exceeded snow extents from the nature
277   run by 26% in the Upper Colorado, 45% in the Great Basin, and 6% in California. Visually, the nature run had significant
278   increases in the spatial variability of winter SWE, better representing the differences in SWE between mountain peaks and
279   valleys, and the patchiness of snow cover in regions with winter snowmelt and ephemeral snow cover (e.g., Fig. 4, Fig. S1).
280   Relative to the nature run, DJF SWE from the open loop simulation was biased high across the full modeling region (Fig. 3)
281   by approximately 26%, on average, with a mean absolute error of 41 mm and spatial coefficient of correlation of approximately
282   0.74. Across the Pacific Northwest (Fig. 4), DJF mean SWE biases were approximately 37%, with a mean absolute error of
283   55 mm. Open loop model performance for the other hydrologic regions can be found in Table 2.
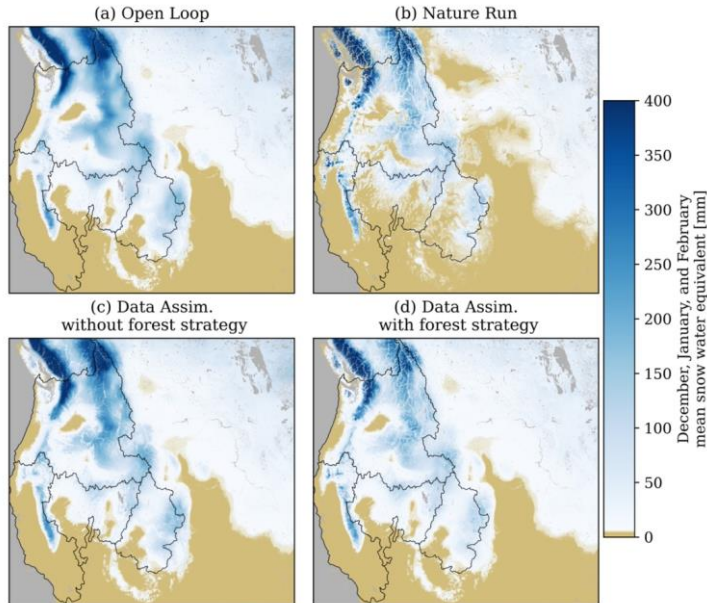
284
285   **Figure 3.** Winter (December, January, and February) mean SWE simulated at 250 m resolution from the open loop (a), nature
286   run (b), and data assimilation simulations, both with (d) and without (c) the forest strategy presented in Sect. 2.4.

287
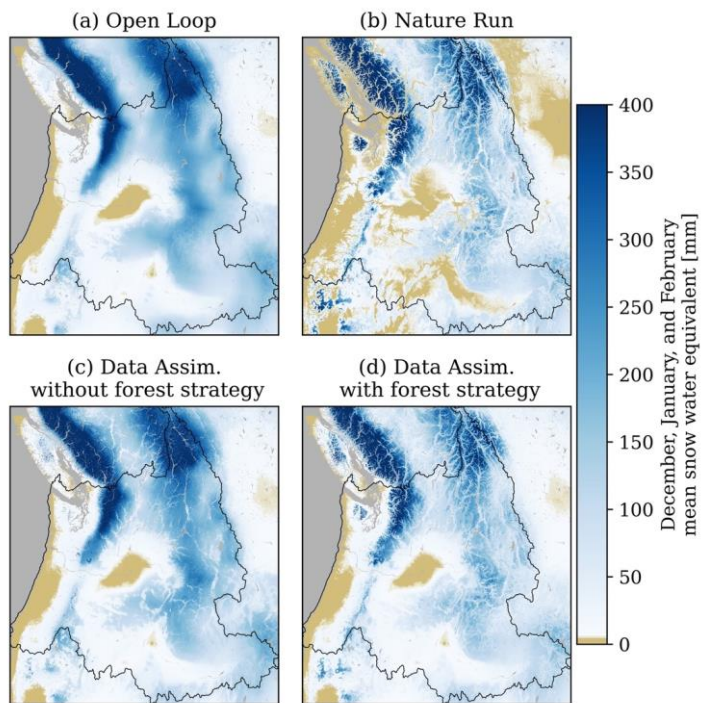
Figure 4. Winter (December, January, and February) mean SWE in the Pacific Northwest region simulated at 250 m
resolution from the open loop (a), nature run (b), and data assimilation simulations, both with (d) and without (c) the forest
strategy.

Table 2. Simulation performance, relative to the nature run simulation, for the open loop simulation (OL) and the simulations with data assimilation, both with (DA+F) and without (DA) the forest strategy. Statistics are presented for the full domain, the four hydrologic regions, and all forested and unforested grid cells.

			13 March 2019 SWE			Seasonal SWE and runoff	
		DJF* snow-extent biases	Mean bias	SWE abs. error [mm]	Coeff. of corr.	MAM* mean SWE bias	Nash-Sutcliffe Efficiency
Full study domain	OL^	+22%	+26%	41	0.74	-	-
	DA^	+23%	+9%	36	0.79	-	-
	DA+F^	+22%	+4%	17	0.91	-	-
Upper Colorado	OL	+26%	+37%	55	0.74	+63%	-2.59
	DA	+28%	+27%	50	0.74	+86%	-3.71
	DA+F	+28%	+8%	23	0.90	< 1%	0.22
Pacific Northwest	OL	+12%	+42%	89	0.69	+44%	-0.17
	DA	+13%	+32%	80	0.74	+80%	-0.34
	DA+F	+13%	+6%	35	0.89	+15%	0.39
Great Basin	OL	+45%	+35%	38	0.62	-29%	0.58
	DA	+46%	+46%	32	0.75	+10%	0.58
	DA+F	+46%	+28%	23	0.83	-38%	0.53
California	OL	+6%	-34%	50	0.64	-50%	0.92
	DA	+8%	-6%	40	0.79	-15%	0.88
	DA+F	+8%	-6%	28	0.88	-26%	0.89
Unforested	OL	+19%	+14%	22	0.83	-	-
	DA	+20%	< 1%	14	0.91	-	-
	DA+F	+20%	< 1%	14	0.91	-	-
Forested	OL	+29%	+150%	111	0.67	-	-
	DA	+30%	+150%	111	0.67	-	-
	DA+F	+30%	+18%	27	0.93	-	-

*DJF = December, January, and February; MAM = March, April, and May (averages)
^ OL = open loop simulation; DA = data assimilation without the forest strategy; DA+F = data assimilation with the forest strategy

As expected, the simulations assimilating the synthetic SWE observations agreed with the nature run better than the open loop simulation. However, on 13 March 2019 (the date of maximum domain SWE volume), the simulation with data assimilation without the forest strategy had high-biased SWE across large portions of the Rocky Mountains and the Cascade Mountain range (Fig. 1, Fig. 5b and Fig. 5e). Low biased SWE was more common in Northernmost Canadian portions of the Rocky Mountains and Cascade Range, the Western montane regions in Washington State, the Northern portions of the Great Basin, and the lower-lying elevations of the California Sierra Nevada. Additionally, despite the assimilation, snow extents were still biased high relative to the nature run (Fig. 3) at magnitudes similar to the open loop simulation (Table 2). This was driven by the expansive snow extents of the open loop simulation, which were decreased by data assimilation, but still resulted in widespread early-season SWE increases for short periods of time between synthetic observations (at 10 – 14 day

303 frequencies), increasing to the number of grid cells with DJF SWE exceeding 5 mm (threshold used to define average winter
304 snow extents in Fig. 3).

305   Assimilating the synthetic SAR observations without the forest strategy best improved SWE in shrub, grass, crop, bare, and
306 wetland landcover types (Fig. 6b and 6c). For example, relative to the open loop simulation (Fig. 5a and 5d), data assimilation
307 without the forest strategy (Fig. 5b and 5e) corrected the high SWE biases in the Great Plains (Fig. 1). While 13 March SWE
308 in shrub, grass, crop, bare-ground, and wetland regions was typically small in magnitude, these landcover types accounted for
309 77% of the modeling domain area, and 61% of the domain total SWE volume on 13 March (Fig. 6a). In these regions, SWE
310 from the open loop simulation had a mean absolute error of 22 mm, and a mean bias of approximately 14%, relative to the
311 nature run (Table 2). Data assimilation significantly improved the SWE bias in these land cover types to within 1%, on average
312 (Fig. 6b), with a mean absolute error of 14 mm, relative to the nature run.
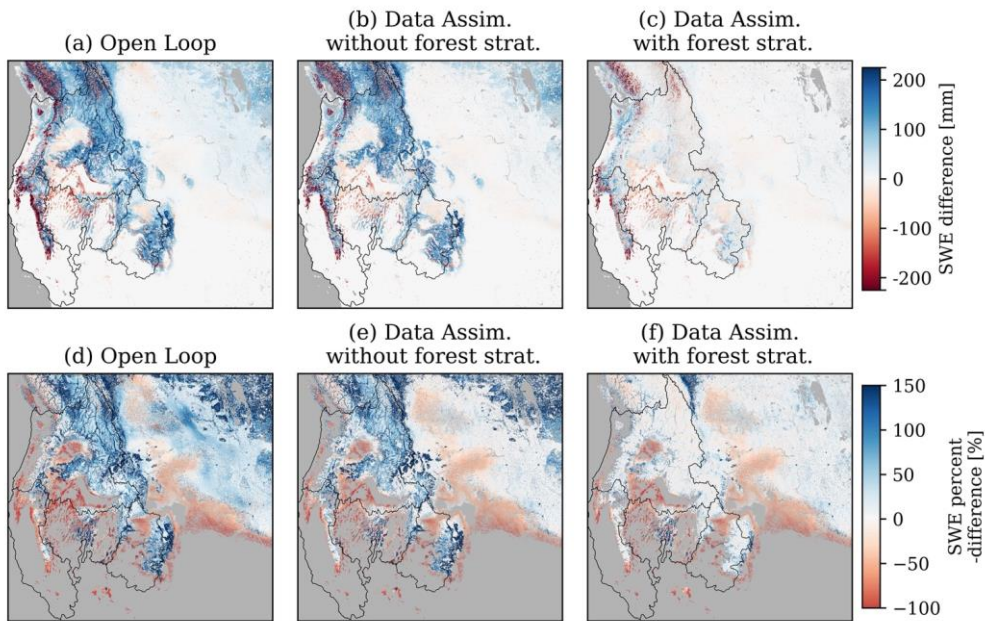
313
314 **Figure 5.** 13 March 2019 SWE difference (top row) and percent-difference (bottom row), relative to the nature run, for the
315 open loop simulation (a and d), and simulations with data assimilation, both with (c and f) and without (b and e) the forest
316 strategy. SWE percent-different maps (bottom row) only compare grid cells where SWE from the nature run was greater
317 than 5 mm.

318   The data assimilation results discussed above did not use the synthetic observations over forested grid cells, where

319   retrievals from SAR instruments may be either partially or fully occluded by the canopy overstory (Tsang et al., 2022; Ruiz

320   et al., 2022; Huang et al., 2019). However, a significant portion of the snow volume in mid-latitude domains overlaps with

321   forests. For example, although forests only covered approximately 22% of the study region investigated here (Fig. 1a),

322   forested grid cells contained just over 34% of the total 13 March SWE volume, a volume about 10% higher than the snow

323   volume contained in the next-largest landcover type (Fig. 6a). In forested grid cells, SWE simulated by the open loop

324   simulation were biased high by approximately 87 mm (+150%) on average (Fig. 6), with a mean absolute error of 111 mm

325   (Table 2). These errors were propagated into the simulation with data assimilation without the forest strategy. Fortunately,

326   the ratio between modeled SWE and synthetic SWE observations in forested grid cells and the nearest canopy-free grid cells

327   had high levels of similarity. Therefore, estimating snow in forest regions using the nearest canopy-free pixels (Fig. 2)

328   improved snow simulations significantly (Fig. 3d, Fig. 4d, and Fig. 5c and 5f). In fact, snow simulated in forest landscapes

329   using data assimilation with the forest strategy agreed well with the nature run, exhibiting a 13 March SWE average bias in

330   forested grid cells of only 14 mm (+8%) (Fig. 6), and a mean absolute error of 27 mm. This forest strategy resulted in large-

331   scale improvements to total domain SWE (Fig. 5), reducing the 13 March full-domain SWE volume bias by 28%, and

332   improving the spatial coefficient of correlation by 0.12, relative to the data assimilation simulation without the forest

333   strategy.
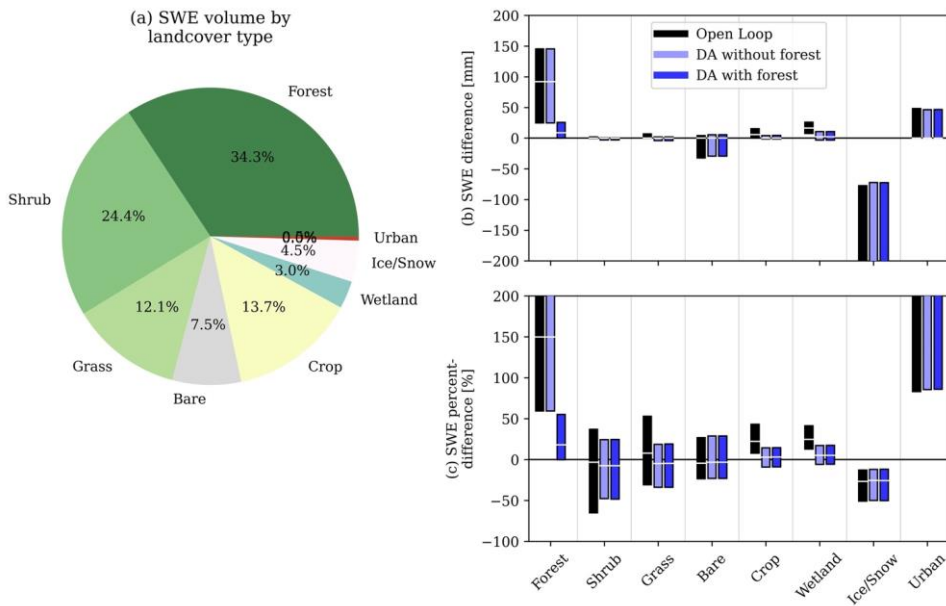
334

335 **Figure 6.** SWE volume on 13 March 2019 broken down by landcover type in subplot a. For each landcover type, the
336 interquartile range and median of SWE differences (b) and SWE percent-differences (c) are calculated for the open loop
337 simulation (black) and each simulation with data assimilation (blue bars). SWE differences (b) and (c) are calculated relative
338 to the nature run.

339   The comparisons above focused on mean DJF SWE and SWE from the date nearest maximum snow volume (13 March,

340 2019). However, assimilating the synthetic SWE data also improved estimates of snow water resources throughout the

341 duration of the water year, even in periods when most snow-covered regions were experiencing snowmelt and synthetic

342 observations were masked. For example, in the Upper Colorado, approximately 75% of the region had DJF snow cover with

343 little or no winter snowmelt (Fig. 7). The simulation with data assimilation and the forest strategy substantially improved

344 mean SWE evolution in the snow accumulation season in this hydrologic region (Fig. 7, October - March). However,

345 snowmelt onset in the March, April, and May (MAM) months increased the number of grid cells experiencing snowmelt

346 from the open loop model outputs, reducing the number of grid cells across the full Upper Colorado Region that could be

347 observed by the synthetic SAR observations to approximately 5%, on average, over this period of time. Despite this, since

348 the simulation with data assimilation improved the volume, timing, and spatial distribution of maximum SWE, mean SWE

349 evolution tracked the nature run simulation significantly better than the open loop simulation in the spring snowmelt period.

350 In fact, relative to the nature run, MAM SWE from the open loop simulations was biased high by approximately 63%, on

351 average, in the Upper Colorado (Table 2). The simulation with data assimilation using the forest strategy improved this bias

352 to less than 1%, on average, over the same period. In this study, simulations using Noah-MP (open loop and data

353 assimilation simulations) melted snow more rapidly in the later-half of the spring snowmelt season than the nature run

354 simulation which evolved SWE using SnowModel (Section 2.1). Therefore, although maximum SWE volume, maximum

355 SWE timing, and MAM SWE were improved by data assimilation, the timing of snow disappearance for the simulation with

356 data assimilation using the forest strategy was approximately 18 days earlier than the nature run in the Upper Colorado.

357
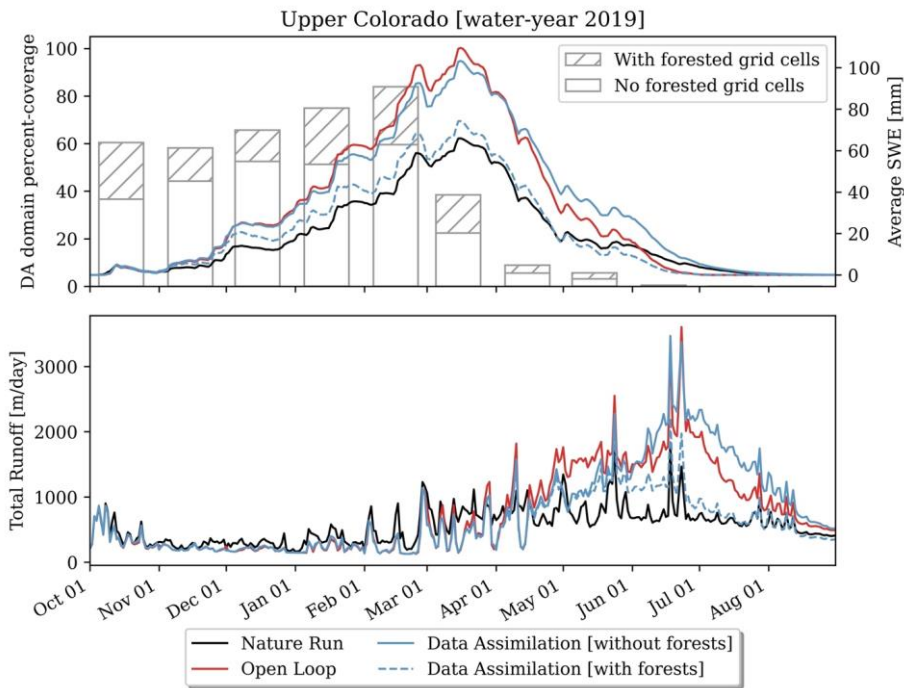
358 **Figure 7.** Time series comparison of mean SWE (top) and total runoff (bottom) between the open loop, nature run, and
359 simulations assimilating the synthetic observations, both with and without the forest strategy in the Upper Colorado. Dashed
360 bars in the top plot represent the monthly percentage of the Upper Colorado grid cells with no snowmelt. Solid bars also
361 exclude grid cells with forest coverage.

362 Much like the Upper Colorado, SWE simulated by the open loop simulation in the Pacific Northwest (Fig. S7) was biased

363 high for the entirety of the snow season. Both domains also had greater than 80% synthetic snow observation coverage in

364 March (including grid cells that filled snow estimates using the forest strategy), and as a result, the simulation with data

365   assimilation using the forest strategy closely matched SWE from the nature run. However, both of these domains had a

366   significant portion of the seasonal snowpack in forested landcover (Fig. 7 and Fig. S7, difference between the hatched and

367   solid bars). These grid cells had winter SWE estimates from the open loop simulation that were predominately high-biased

368   (Fig. 3 and Fig. 5). Therefore, although data assimilation improved winter SWE in non-forested landcover types (Fig. 6), the

369   simulation without the forest strategy caused little-to-no improvement in the simulated domain mean maximum SWE (Table

370   2). This highlights the value of the forest strategy used here (Fig. 2), which drew information from synthetic observations in

371   relatively few nearby pixels to infer the mean snow volume in forested grid cells. Given the four hydrologic regions

372   investigated in this study, a far smaller volume of snow existed in forested landcover for the California (Fig. S8) and Great

373   Basin regions (Fig. S6), resulting in DJF domain-mean SWE evolution that was more similar between the simulations with

374   and without the forest strategy. We expect results in these domains to be more indicative of the value of winter SAR

375   observations in less-vegetated snowy landscapes, such as Tundra and Prairie snow regimes (Sturm and Liston, 2021).

376   Finally, the improvements to the spatial and temporal estimates of SWE discussed above had trickle-down improvements

377   on simulated runoff. For example, in the Upper Colorado (Fig. 7), total annual runoff from the open loop simulation was

378   biased high by approximately 35%, relative to the nature run. This error was driven most by high-biased winter snow

379   accumulation, which nearly doubled the melt season (March – July) runoff estimated by the nature run simulation. Here, by

380   assimilating the synthetic SWE observations, and estimating forest snowpack from the relationship between modeled and

381   observed SWE from the nearest canopy-free pixels, total annual streamflow in this domain was improved to within 1%. Not

382   only was domain total runoff improved, but the seasonal evolution of high and low-flows vital for water management and

383   planning was also improved. This improved the Nash-Sutcliffe Efficiency (NSE) from –2.59 to 0.22 between the open loop

384   simulation and simulation with data assimilation employing the forest strategy (Table 2). These results were similar for the

385   Pacific Northwest, which had an NSE that improved from –0.17 to 0.39. However, due to the smaller changes to SWE and

386   more-rapid snowmelt simulated by Noah-MP, changes to runoff from data assimilation in California and the Great Basin

387   were small (Table 2), with improvements that were largely outweighed by the difference in snowmelt timing and rates

388   between Noah-MP and SnowModel.

389   **4. Discussion**

390   The differences between the open loop simulation and nature run in this study were representative of snow modeling errors

391   common for continental and global-scale models used for seasonal to long-term future snow predictions (e.g., Franz et al.,

392   2010; Garousi-Nejad and Tarboton, 2022; Kim et al, 2021; Liu et al, 2022). The greatest source of these snow modeling errors

393   is commonly errors in meteorological forcing data, and in particular, biases in precipitation (Garousi-Nejad and Tarboton,

394   2022; Henn et al., 2018; Pflug et al., 2021; Raleigh and Lundquist, 2012; Wayand et al., 2013). These biases are especially

395   prevalent in the portions of the earth's surface with the greatest volumes of snow, such as the tundra and montane regions (Kim

396   et al., 2021), where ground observations and observation station maintenance are hindered by harsh winter conditions and

397 inaccessibility. This suggests that the greatest need for improving global estimates of snow is improved estimates of snow
398 accumulation in remote, under sampled landscapes. Here, we expect that the SAR observations evaluated in this study could
399 address these needs, thus providing a path forward for pairing common snow models with observations as a basis for
400 determining global snow mass. For example, assimilating SAR observations at 10 – 14 day intervals with the observational
401 error characteristics reported in Sect. 2.2, improved midlatitude winter SWE volume by approximately 22%, on average (Table
402 2). In unforested landscapes, which account for a majority of the Earth's snow water storage (Kim et al., 2021), assimilation
403 improved the mean SWE bias at maximum SWE timing to within 1%, on average, and reduced the standard deviation of errors
404 by approximately 45 mm (~85%) (Fig. 6).

405 Despite the benefits discussed above, SAR observations have known limitations in forested landscapes where the canopy
406 overstory obstructs retrievals from the underlying snowpack (Huang et al., 2019; Ruiz et al., 2022; Tsang et al., 2022).
407 Therefore, this study was designed to investigate a forest strategy that uses the relationship between modeled SWE estimates
408 and synthetic SWE observations from neighboring grid cells as the basis for inferring snow distribution in regions with forested
409 landcover (Fig. 2). To focus on the benefits of this approach, we chose a domain (Fig. 1) that included both significant forest
410 spatial coverage (22%) with disproportionate amounts of winter snow (34%) within the forested pixels (Fig. 6). Relative to the
411 open loop simulation, the simulation with data assimilation and the forest strategy dramatically improved the spatial
412 distribution of SWE (e.g., Fig. 3 and Fig. 4) and the resulting SWE biases at domain maximum snowpack timing (Fig. 5). In
413 fact, in forested grid cells, SWE on 13 March was only biased by 14 mm (mean absolute error of 27 mm), on average, for the
414 simulation with data assimilation and the forest strategy, relative to the nature run. This was opposed to the open loop
415 simulation, which was biased by 87 mm (mean absolute error of 111 mm) over the same regions and date. Despite the fact that
416 the two simulations with data assimilation agreed in all grid cells except forested grid cells, the simulation employing the forest
417 strategy had a mean absolute error (17 mm) across the full modeling region that was approximately 51% smaller than the
418 simulation without the forest strategy. Here, we recognize that this study used a single date (13 March) to represent snow water
419 resources at maximum SWE timing. However, the date of maximum SWE volume from the nature run varied by less than a
420 week across the four hydrologic regions (11 - 16 March; Fig. 7, Fig. S6 - S8). Therefore, this was a relevant date for model
421 comparisons, especially given that water resource and allocation decisions in the Western US are often based on the volume
422 of snow at maximum snow timing.

423 This research shows how a modeling framework and relatively few observations can be used to gap-fill estimates of snow
424 in regions where remote sensing observations from a future platform may be most challenged. Despite the fact that snowpack
425 with properties able to be retrieved by SAR instrumentation (i.e., canopy-free landcover and no snowmelt) sometimes only
426 accounted for only small portions of a modeling domain (e.g., Fig. 7), SWE from the model and SAR observations in nearby
427 canopy-free grid cells were predictive of the snow in forested grid cells. We hypothesize that this could have partly been driven
428 by the 250 m resolution of synthetic observations and simulations. At this length scale, snow distribution is typically driven

429 by processes like mesoscale weather patterns and their interaction (e.g., orographic lapse rates, wind loading/sheltering, terrain-

430 shading, etc.) with static topographical features like elevation, slope, and aspect (e.g., Clark et al., 2011; Lehning et al., 2011;

431 McGrath et al., 2018; Minder et al., 2008; Trujillo et al., 2007). However, we acknowledge that snow in forested and open grid

432 cells is subject to different snow processes. In fact, the nature run simulation used here attempts to simulate snow-canopy

433 interactions, such as snow interception and solar shading from the canopy overstory (Liston and Elder, 2006). Here, since we

434 focus predominantly on model improvements from data assimilation in the SWE accumulation season, we hypothesize that

435 the primary difference between SWE accumulation in forested pixels, and the nearest canopy-free grid cells could be driven

436 by canopy interception, or the lack thereof. In other words, inferring forested snowpack using the nearest canopy-free grid

437 cells could bias snow in forested regions where snow processes differ slightly. While the forest strategy improved SWE

438 simulated in forested grid cells at the date of maximum SWE volume, SWE was still biased high relative to the nature run

439 (Fig. 6). We hypothesize that a correction factor, based on variables like forest canopy type, vegetation density, wind speed,

440 and temperature during snowfall, all of which influence snow interception (Lundquist et al., 2021), could be used to facilitate

441 the difference in snow accumulation expected between a forest pixel and SWE observations from nearby canopy-free grid

442 cells. This approach will be a topic of future research. However, since errors with precipitation are often the overwhelming

443 source of model errors, we hypothesize that the forest strategy (Fig. 2), which corrected modeled SWE in forested areas using

444 the ratio between modeled and observed SWE in nearby open areas, was well-suited to correct precipitation biases.

445 The results presented here are subject to a number of assumptions. These assumptions were intended to apply regionally-

446 consistent and conservative rules about how 1) synthetic SAR observations were generated, and 2) the grid cells and time

447 periods that SAR observations occurred in. For example, we used a 20% and zero-mean random distribution of errors to

448 generate observations from the nature run. We expect the error from a future satellite mission to be less than 20% over the

449 majority of snow covered regions (Sect. 2.2). However, observational biases may be more common in certain locations and

450 periods based on snow depth, particularly in very shallow or very deep snowpacks, terrain characteristics and vegetation

451 characteristics. Additionally, the landcover classification used in this study (Fig. 1) was based on the dominant landcover type

452 within each model grid cell, as defined from the North American Land Change Monitoring System (Latifovic et al., 2017). For

453 forested grid cells, this included needleleaf, broadleaf, and mixed forest types. To be conservative, this study completely

454 masked synthetic observations in 250 m grid cells classified as forest, thereby assuming 1) no observation capabilities in

455 predominantly forested areas, and 2) full observation capabilities in grid cells where forests were not the dominant landcover

456 type. In reality, SAR may be able to achieve accurate snow retrievals in some forested-dominated regions based on the forest

457 type, forest distribution, and canopy density (Tsang et al., 2022). Conversely, some regions with sparser or no forest cover

458 may still have observation limitations based on the domain and snow characteristics mentioned above. The large domain used

459 in this study also made tests over multiple years computationally challenging. Here, the intent of this study was to investigate

460 a strategy for deriving SWE corrections in difficult to observe forest landscapes, and we hypothesize that precipitation biases

461 and the resulting modeled SWE accumulation could be improved to a similar degree in years with both larger and smaller

462 snow volumes. Finally, while strategies for identifying and correcting systematic SAR observation errors are a topic of
463 continued research (e.g., Durand et al., 2023; Singh et al., 2023), OSSEs are an inherently flexible framework for evaluating
464 sensor utility, so future research could use the simulations performed here to test a wider array of sensor configurations and
465 non-normal retrieval errors. Future work could build upon these results to investigate multiple years, perhaps considering
466 warmer and/or drier snow years, when the role of snowpack for water supply and midwinter snowmelt and rain-on-snow
467 frequency may be more likely to increase snowpack liquid water content, or years with late-season spring snow accumulation.
468 Future research should also investigate other gap-filling approaches, like methods to infer SWE in grid cells where snowmelt
469 is occurring and liquid water may prevent SAR retrievals, and gap-filling approaches using different window sizes and/or
470 searching windows that more heavily weight unforested grid cells with similar characteristics (elevation, aspect, etc.).

471   This study tested a simple model setup using a popular land surface model (Noah-MP) and Kalman-based data assimilation
472 procedure. This data assimilation procedure updated modeled snow states, like snow depth and SWE, based only on synthetic
473 SWE observations at 10 – 14 day temporal frequencies where/when snowmelt was not occurring. Despite the limitations and
474 assumptions discussed above, we expect that the results presented here could represent the lower-bound of performance that
475 could be achieved from a real-time modeling framework that could accompany a space-borne SAR remote sensing platform.
476 For example, many studies have demonstrated repeatable patterns of snow accumulation in years with similar winter
477 meteorological characteristics (e.g., Deems et al., 2008; Pflug et al, 2022; Schirmer et al., 2011; Sturm and Wagner, 2010;
478 Woodruff and Qualls, 2019). This suggests that retrospective information about snow distribution patterns in previous years,
479 could be used as the basis for extrapolating and updating snow model states in grid cells not covered by SAR observations on
480 a given date. From the modeling perspective, only 5 ensemble members were used in the Ensemble-Kalman data assimilation
481 (Sec 2.3), when a larger ensemble of simulations may have improved uncertainty characterization of simulated snow and
482 hydrological states even more. This study also assumed that synthetic SAR observations were unable to observe snow in all
483 forested landscapes, when retrievals of snow in forested stands could be achievable for some forested regions with smaller tree
484 cover fractions and biomass (Montomoli et al., 2015; Tsang et al., 2022). Finally, the SAR configuration tested here had 10 –
485 14 day repeat times, but future satellite configurations with more-frequent observational repeats are possible and have been
486 recommended by the 2018 Decadal Survey (NASEM 2018). Despite all of these conservative assumptions, the difference
487 between the open loop simulation (representative of current modeling accuracies), and the simulation with synthetic
488 observation data assimilation using the forest strategy, demonstrated large-magnitude and widespread improvements to real-
489 time estimates of winter SWE and the associated improvement to spring SWE and runoff. Therefore, we expect the findings
490 of this study, particularly the strategy to extend the observational utility to forested areas, to significantly aid in the full
491 exploitation of the information from a future SAR-based snow satellite mission.

492 5. **Conclusion**

493   Global estimates of snow volume and distribution have uncertainties stemming from limited snow observations and

494   biases in meteorological forcing data. These uncertainties stress the need for a global snow-focused satellite remote

495   sensing platform. Here, we investigate the degree to which synthetic observations of SWE representative of a Synthetic

496   Aperture Radar (SAR) remote sensing platform, could correct common snow modeling errors and provide

497   spatiotemporally continuous SWE estimates. We investigate this using an Observing System Simulation Experiment,

498   specifically investigating how much snow simulated using a widely used land surface model and meteorological forcing

499   dataset, could be improved by assimilating synthetic SAR observations of SWE.

500   The difference between the open loop simulation and the nature run was representative of common modeling errors.

501   Snow simulated by the open loop simulation had larger winter snow extents, and total snow volume that was biased high

502   by approximately 35%. The open loop simulation also simulated snow that was more spatially homogeneous,

503   underestimating the variability across variations in topography and underestimating lower-elevation snowmelt from the

504   nature run. Assimilating the synthetic SWE observations improved SWE simulated in the shrub, grass, crop, bare-ground,

505   and wetland land cover types. In fact, SWE biases on the date of domain maximum SWE volume (13 March 2019) in

506   these landcover types improved from 14% for the open loop simulation to within 1% after data assimilation. However,

507   despite only covering 22% of the study area, forested grid cells contained just over 34% of the domain SWE on 13

508   March. The open loop simulation and the simulation with data assimilation without the forest strategy had SWE that was

509   high biased by 150% (87 mm), on average, in these forested grid cells. The relationship between modeled SWE and

510   synthetic SWE observations in forested grid cells exhibited similarities with the nearest canopy-free grid cells. Therefore,

511   SWE in forested regions was able to be inferred using the simple modeling framework and synthetic SAR observations

512   from nearby canopy-free grid cells. In fact, the simulation with data assimilation using this forest gap-filling strategy

513   substantially improved SWE biases to 4% (~22% improvement) at maximum SWE timing, with a SWE mean absolute

514   error of 17 mm (24 mm improvement) and spatial correlation of 0.91 (0.17 improvement) across the Western US

515   Improvements in winter SWE accumulation also improved estimates of melt-season SWE evolution and total runoff

516   in four major Western US hydrologic regions, even in periods when winter snowmelt greatly reduced the number of grid

517   cells that could be observed by the synthetic SWE observations. In fact, in the Upper Colorado River, melt season SWE

518   biases improved from 63% to less than 1% after assimilation, and the runoff Nash Sutcliffe Efficiency improved from -

519   2.59 to 0.22. These results demonstrate the value of SAR observations and simple spatial-filling strategies in grid cells

520   where SAR retrievals could be obstructed by the canopy. Here, we expect our results to represent a lower-boundary of

521   model performance which could be improved further by more robust assimilation approaches, more-frequent SAR

522   observations, further developments to SAR retrieval algorithms in forested landscapes, and adaptations to the forest gap-

523 filling strategy developed here. However, our results also show that widespread improvements to global SWE could be

524 available in near real-time provided data assimilation approaches and a SAR remote sensing platform.

525 *Code availability:* The Land Information System (LIS; lis.gsfc.nasa.gov) framework used to perform the nature run, open

526 loop, and data assimilation simulations from this study can be accessed from a GitHub public repository

527 (https://github.com/NASA-LIS/LISF). Model documentation and LIS tutorials can also be accessed from this repository. Users

528 are encouraged to reference Kumar et al. (2006) for more information on LIS. The Trade-space Analysis Tool for designing

529 Constellations (TAT-C) tool is currently available on-request for federal employees and contractors

530 (https://software.nasa.gov/software/GSC-18399-1).

531 *Data availability:* The model outputs and data necessary to reproduce the figures and statistics reported in this study can

532 be found at https://www.hydroshare.org/resource/e0ad80f818bf4062a335e9e0d7362834/. This repository includes

533 domain static variables, such as land cover, elevation, and spatial coordinates, in addition to model outputs of winter-average

534 SWE, SWE at the date of maximum SWE volume (13 March 2019), and SWE and runoff aggregated across each region.

535 MERRA-2 forcing data can be accessed from the Goddard Earth Sciences Data and Information Services Center (GES DISC,

536 https://disc.gsfc.nasa.gov/), and ERA5 data can be accessed from the European Centre for Medium-Range Weather Forecasts

537 climate data store (https://www.ecmwf.int/en/forecasts/dataset/ecmwf-reanalysis-v5).

538 *Author contributions:* CV and SK coordinated the manuscript question and research methodology. SK adapted LIS model

539 source code to implement the forest gap-filling strategy in Sect. 2.4. MW set up the model domains and model configurations,

540 and performed the open loop simulation. EC assisted with generating the synthetic SWE observations. With assistance from

541 KA, JP performed code developments for the simulations using both the Noah-MP and coupled SnowModel models. KA

542 implemented the SnowModel code and parameters into LIS and LDT. JP also performed the nature run and both data

543 assimilation simulations. The manuscript was written provided text, figures, and feedback from all coauthors.

544 *Competing interests:* The authors declare that they have no conflict of interest.

545 *Acknowledgements:* This work was supported by the funding from the NASA Terrestrial Hydrology program. Computing was

546 supported by the NASA Center for Climate Simulation (NCCS). We would also like to acknowledge Dr. Ethan Gutmann and

547 NASA Grant 80NSSC20K0207 for supporting the integration of the SnowModel distributed model into LIS.

548 **References**

549 Arsenault, K.R., Wrzesien, M., Gutmann, E.D., Vuyovich, C., Liston, G.E., Mower, R., Reinking, A., Newman, A.J., Kumar,
550   S.V., Wang, S., Navari, M., Forman, B.A., Jessica, L.: Implementing SnowModel into the Land Information System
551   Framework to Support High Resolution Modeling of Snow Heterogeneity. Presented at the AGU Fall Meeting 2021,
552   AGU, 2021.

553 Barnett, T.P., Adam, J.C., Lettenmaier, D.P.:Potential impacts of a warming climate on water availability in snow-dominated
554   regions. Nature 438, 303. https://doi.org/10.1038/nature04141, 2005.
555 Barry, R.G.: The Role of Snow and Ice in the Global Climate System: A Review. Polar Geography 26, 235–246.
556   https://doi.org/10.1080/789610195, 2002.
557 Best, M.J., Pryor, M., Clark, D.B., Rooney, G.G., Essery, R.L.H., Ménard, C.B., Edwards, J.M., Hendry, M.A., Porson, A.,
558   Gedney, N., Mercado, L.M., Sitch, S., Blyth, E., Boucher, O., Cox, P.M., Grimmond, C.S.B., Harding, R.J.: The Joint
559   UK Land Environment Simulator (JULES), model description – Part 1: Energy and water fluxes. Geoscientific Model
560   Development 4, 677–699. https://doi.org/10.5194/gmd-4-677-2011, 2011.
561 Beven, K.J., Kirby, M.J., Freer, J.E., Lamb, R.: A history of TOPMODEL. Hydrology and Earth System Sciences 25, 527 549.
562   https://doi.org/10.5194/hess-25-527-2021, 2021.
563 Cho, E., Vuyovich, C. M., Kumar, S. V., Wrzesien, M. L., & Kim, R. S. (2023). Evaluating the utility of active microwave
564   observations as a snow mission concept using observing system simulation experiments. The Cryosphere, 17(9),
565   3915-3931.
566 Clark, M.P., Hendrikx, J., Slater, A.G., Kavetski, D., Anderson, B., Cullen, N.J., Kerr, T., Hreinsson, E.Ö., Woods, R.A.:
567   Representing spatial variability of snow water equivalent in hydrologic and land-surface models: A review. Water
568   Resources Research 47. https://doi.org/10.1029/2011WR010745, 2011.
569 Cosgrove, B.A., Lohmann, D., Mitchell, K.E., Houser, P.R., Wood, E.F., Schaake, J.C., Robock, A., Marshall, C., Sheffield,
570   J., Duan, Q., Luo, L.: Real-time and retrospective forcing in the North American Land Data Assimilation System
571   (NLDAS) project. Journal of Geophysical Research: Atmospheres, 108.D22, 2003.
572 De Lannoy, G.J.M., Reichle, R.H., Arsenault, K.R., Houser, P.R., Kumar, S., Verhoest, N.E.C., Pauwels, V.R.N.: Multiscale
573   assimilation of Advanced Microwave Scanning Radiometer–EOS snow water equivalent and Moderate Resolution
574   Imaging Spectroradiometer snow cover fraction observations in northern Colorado. Water Resources Research 48.
575   https://doi.org/10.1029/2011WR010588, 2012.
576 Deems, J.S., Fassnacht, S.R., Elder, K.J.: Interannual Consistency in Fractal Snow Depth Patterns at Two Colorado Mountain
577   Sites. J. Hydrometeor 9, 977–988. https://doi.org/10.1175/2008JHM901.1, 2008.
578 Derksen, C., Lemmetyinen, J., Toose, P., Silis, A., Pulliainen, J., Sturm, M.: Physical properties of arctic versus subarctic
579   snow: Implications for high latitude passive microwave snow water equivalent retrievals. Journal of Geophysical
580   Research: Atmospheres 119, 7254 – 7270. https://doi.org/10.1002/2013JD021264, 2014.
581 Durand, M., Johnson, J.T., Dechow, J., Tsang, L., Borah, F., Kim, E.J.: Retrieval of SWE from dual-frequency radar
582   measurements: Using time series to overcome the need for accurate a priori information. EGUsphere 1 – 23.
583   https://doi.org/10.5194/egusphere-2023-1653, 2023.
584 Ek, M.B., Mitchell, K.E., Lin, Y., Rogers, E., Grunmann, P., Koren, V., Gayno, G., Tarpley, J.D.: Implementation of Noah
585   land surface model advances in the National Centers for Environmental Prediction operational mesoscale Eta model.
586   Journal of Geophysical Research: Atmospheres 108. https://doi.org/10.1029/2002JD003296, 2003.
587 Errico, R.M., Yang, R., Masutani, M., Woollen, J.S.: The estimation of analysis error characteristics using an observation
588   systems simulation experiment. Meteorologische Zeitschrift 16, 695–708, 2007.
589 Fang, Y., Liu, Y., Margulis, S.A.: A western United States snow reanalysis dataset over the Landsat era from water eyars 1985
590   to 2021. Sci Data 9, 677. https://doi.org/10.1038/s41597-022-01768-7, 2022.
591 Foster, J.L., Sun, C., Walker, J.P., Kelly, R., Chang, A., Dong, J., Powell, H.: Quantifying the uncertainty in passive microwave
592   snow water equivalent observations. Remote Sensing of the Environment 94, 187 – 203.
593   https://doi.org/10.1016/j.rse.2004.09.012, 2005.
594 Franz, K.J., Butcher, P., Ajami, N.K.: Addressing snow model uncertainty for hydrologic prediction. Advances in Water
595   Resources 33, 820–832. https://doi.org/10.1016/j.advwatres.2010.05.004, 2010.
596 Garnaud, C., Bélair, S., Carrera, M.L., Derksen, C., Bilodeau, B., Abrahamowicz, M., Gauthier, N., Vionnet, V.: Quantifying
597   Snow Mass Mission Concept Trade-Offs Using an Observing System Simulation Experiment. Journal of
598   Hydrometeorology 20, 155–173. https://doi.org/10.1175/JHM-D-17-0241.1, 2019.
599 Garousi-Nejad, I., Tarboton, D.G.: A comparison of National Water Model retrospective analysis snow outputs at snow
600   telemetry sites across the Western United States. Hydrological Processes 36, e14469.
601   https://doi.org/10.1002/hyp.14469, 2022.

Gelaro, R., McCarty, W., Suárez, M.J., Todling, R., Molod, A., Takacs, L., Randles, C.A., Darmenov, A., Bosilovich, M.G., Reichle, R., Wargan, K., Coy, L., Cullather, R., Draper, C., Akella, S., Buchard, V., Conaty, A., Silva, A.M. da, Gu, W., Kim, G.-K., Koster, R., Lucchesi, R., Merkova, D., Nielsen, J.E., Partyka, G., Pawson, S., Putman, W., Rienecker, M., Schubert, S.D., Sienkiewicz, M., Zhao, B.: The Modern-Era Retrospective Analysis for Research and Applications, Version 2 (MERRA-2). Journal of Climate 30, 5419–5454. https://doi.org/10.1175/JCLI-D-16-0758.1, 2017.

Henn, B., Newman, A.J., Livneh, B., Daly, C., Lundquist, J.D.: An assessment of differences in gridded precipitation datasets in complex terrain. Journal of Hydrology 556, 1205–1219. https://doi.org/10.1016/j.jhydrol.2017.03.008, 2018.

Hersbach, H., Bell, B., Berrisford, P., Hirahara, S., Horányi, A., Muñoz-Sabater, J., Nicolas, J., Peubey, C., Radu, R., Schepers, D., Simmons, A., Soci, C., Abdalla, S., Abellan, X., Balsamo, G., Bechtold, P., Biavati, G., Bidlot, J., Bonavita, M., De Chiara, G., Dahlgren, P., Dee, D., Diamantakis, M., Dragani, R., Flemming, J., Forbes, R., Fuentes, M., Geer, A., Haimberger, L., Healy, S., Hogan, R.J., Hólm, E., Janisková, M., Keeley, S., Laloyaux, P., Lopez, P., Lupu, C., Radnoti, G., de Rosnay, P., Rozum, I., Vamborg, F., Villaume, S., Thépaut, J.-N.: The ERA5 global reanalysis. Quarterly Journal of the Royal Meteorological Society 146, 1999–2049. https://doi.org/10.1002/qj.3803, 2020.

Hiemstra, C.A., Liston, G.E., Reiners, W.A.: Snow Redistribution by Wind and Interactions with Vegetation at Upper Treeline in the Medicine Bow Mountains, Wyoming, U.S.A. Arctic, Antarctic, and Alpine Research 34, 262–273. https://doi.org/10.1080/15230430.2002.12003493, 2002.

Huang, H., Tsang, L., Colliander, A., Yueh, S.H.: Propagation of Waves in Randomly Distributed Cylinders Using Three-Dimensional Vector Cylindrical Wave Expansions in Foldy–Lax Equations. IEEE Journal on Multiscale and Multiphysics Computational Techniques 4, 214–226. https://doi.org/10.1109/JMMCT.2019.2948022, 2019.

Kim, R.S., Kumar, S., Vuyovich, C., Houser, P., Lundquist, J., Mudryk, L., Durand, M., Barros, A., Kim, E.J., Forman, B.A., Gutmann, E.D., Wrzesien, M.L., Garnaud, C., Sandells, M., Marshall, H.-P., Cristea, N., Pflug, J.M., Johnston, J., Cao, Y., Mocko, D., Wang, S.: Snow Ensemble Uncertainty Project (SEUP): quantification of snow water equivalent uncertainty across North America via ensemble land surface modeling. The Cryosphere 15, 771–791. https://doi.org/10.5194/tc-15-771-2021, 2021.

Koster, R.D., Mahanama, S.P.P., Livneh, B., Lettenmaier, D.P., Reichle, R.H.: Skill in streamflow forecasts derived from large-scale estimates of soil moisture and snow. Nature Geosci 3, 613–616. https://doi.org/10.1038/ngeo944, 2010.

Koster, R.D., Suarez, M.J., Ducharne, A., Stieglitz, M., Kumar, P.: A catchment-based approach to modeling land surface processes in a general circulation model: 1. Model structure. Journal of Geophysical Research: Atmospheres 105, 24809–24822. https://doi.org/10.1029/2000JD900327, 2000.

Kumar, S.V., Kolassa, J., Reichle, R., Crow, W., de Lannoy, G., de Rosnay, P., MacBean, N., Girotto, M., Fox, A., Quaife, T., Draper, C., Forman, B., Balsamo, G., Steele-Dunne, S., Albergel, C., Bonan, B., Calvet, J.-C., Dong, J., Liddy, H., Ruston, B.: An Agenda for Land Data Assimilation Priorities: Realizing the Promise of Terrestrial Water, Energy, and Vegetation Observations From Space. Journal of Advances in Modeling Earth Systems 14, e2022MS003259. https://doi.org/10.1029/2022MS003259, 2022.

Kumar, S.V., Peters-Lidard, C.D., Tian, Y., Houser, P.R., Geiger, J., Olden, S., Lighty, L., Eastman, J.L., Doty, B., Dirmeyer, P., Adams, J., Mitchell, K., Wood, E.F., Sheffield, J.: Land information system: An interoperable framework for high resolution land surface modeling. Environmental Modelling & Software 21, 1402–1415. https://doi.org/10.1016/j.envsoft.2005.07.004, 2006.

Kumar, S.V., Peters-Lidard, C.D., Mocko, D., Tian, Y.: Multiscale Evaluation of the Improvements in Surface Snow Simulation through Terrain Adjustments to Radiation. Journal of Hydrometeorology 14, 220–232. https://doi.org/10.1175/JHM-D-12-046.1, 2013.

Kwon, Y., Yoon, Y., Forman, B.A., Kumar, S.V., Wang, L.: Quantifying the observational requirements of a space-borne LiDAR snow mission. Journal of Hydrology 601, 126709. https://doi.org/10.1016/j.jhydrol.2021.126709, 2021.

Lahmers, T.M., Kumar, S.V., Rosen, D., Dugger, A., Gochis, D.J., Santanello, J.A., Gangodagamage, C., Dunlap, R.: Assimilation of NASA's Airborne Snow Observatory Snow Measurements for Improved Hydrological Modeling: A Case Study Enabled by the Coupled LIS/WRF-Hydro System. Water Resources Research 58, e2021WR029867. https://doi.org/10.1029/2021WR029867, 2022.

Latifovic, R., Pouliot, D., Olthof, I.: Circa 2010 Land Cover of Canada: Local optimization methodology and product development. Remote Sensing 9, 11. https://doi.org/10.3390/rs9111098, 2017.

652 Le Moigne, J., Dabney, P., de Weck, O., Foreman, V., Grogan, P., Holland, M., Hughes, S., Nag, S.: Tradespace analysis tool
653   for designing constellations (TAT-C), in: 2017 IEEE International Geoscience and Remote Sensing Symposium
654   (IGARSS). IEEE, pp. 1181–1184, 2017.
655 Lehning, M., Grünewald, T., Schirmer, M.: Mountain snow distribution governed by an altitudinal gradient and terrain
656   roughness. Geophysical Research Letters 38. https://doi.org/10.1029/2011GL048927, 2011.
657 Li, D., Wrzesien, M.L., Durand, M., Adam, J., Lettenmaier, D.P.: How much runoff originates as snow in the western United
658   States, and how will that change in the future? Geophysical Research Letters 44, 6163–6172.
659   https://doi.org/10.1002/2017GL073551, 2017.
660 Liang, X., Lettenmaier, D.P., Wood, E.F., Burges, S.J.: A simple hydrologically based model of land surface water and energy
661   fluxes for general circulation models. Journal of Geophysical Research: Atmospheres 99, 14415–14428.
662   https://doi.org/10.1029/94JD00483, 1994.
663 Lievens, H., Demuzere, M., Marshall, H.P., Reichle, R.H., Brucker, L., de Rosnay, P., Dumont, M., Girotto, M., Immerzeel,
664   W.W., Jonas, T., Kim, E.J., Koch, I., Marty, C., Saloranta, T., Schober, J., De Lannoy, G.J.M.: Snow depth variability
665   in the Northern Hemisphere mountains observed from space. Nature Communications, 2019.
666 Liston, G.E., Elder, K.: A Distributed Snow-Evolution Modeling System (SnowModel). Journal of Hydrometeorology 7,
667   1259–1276. https://doi.org/10.1175/JHM548.1, 2006.
668 Liston, G.E., Perham, C.J., Shideler, R.T., Cheuvront, A.N.: Modeling snowdrift habitat for polar bear dens. Ecological
669   Modelling 320, 114–134. https://doi.org/10.1016/j.ecolmodel.2015.09.010, 2016.
670 Liu, Y., Fang, Y., Li, D., Margulis, S.A.: How well do global snow products characterize snow storage in high mountain Asia?
671   Geophysical Research Letters 49, e2022GL100082. https://doi.org/10.1029/2022GL100082, 2022.
672 Livneh, B., Badger, A.M.: Drought less predictable under declining future snowpack. Nat. Clim. Chang. 10, 452–458.
673   https://doi.org/10.1038/s41558-020-0754-8, 2020.
674 Lundquist, J.D., Dickerson-Lange, S., Gutmann, E., Jonas, T., Lumbrazo, C., Reynolds, D.: Snow interceptions modelling:
675   Isolated observations have led to many land surface models lacking appropriate temperature sensitivities.
676   Hydrological Processes 35, 7. https://doi.org/10.1002/hyp.14274, 2021.
677 Mahoney, P.J., Liston, G.E., LaPoint, S., Gurarie, E., Mangipane, B., Wells, A.G., Brinkman, T.J., Eitel, J.U.H., Hebblewhite,
678   M., Nolin, A.W., Boelman, N., Prugh, L.R.: Navigating snowscapes: scale-dependent responses of mountain sheep
679   to snowpack properties. Ecological Applications 28, 1715–1729. https://doi.org/10.1002/eap.1773, 2018.
680 McGrath, D., Sass, L., O'Neel, S., McNeil, C., Candela, S.G., Baker, E.H., Marshall, H.P.: Interannual snow accumulation
681   variability on glaciers derived from repeat, spatially extensive ground-penetrating radar surveys. The Cryosphere 12,
682   3617–3633. https://doi.org/10.5194/tc-12-3617-2018, 2018.
683 Mernild, S.H., Liston, G.E., Hiemstra, C., Wilson, R.: The Andes Cordillera. Part III: glacier surface mass balance and
684   contribution to sea level rise (1979–2014). International Journal of Climatology 37, 3154–3174.
685   https://doi.org/10.1002/joc.4907, 2017.
686 Minder, J.R., Durran, D.R., Roe, G.H., Anders, A.M.: The climatology of small-scale orographic precipitation over the
687   Olympic Mountains: Patterns and processes. Quarterly Journal of the Royal Meteorological Society 134, 817–839.
688   https://doi.org/10.1002/qj.258, 2008.
689 Montomoli, F., Macelloni, G., Brogioni, M., Lemmetyinen, J., Cohen, J., Rott, H.: Observations and simulation of
690   multifrequency SAR data over a snow-covered boreal forest. IEEE journal of selected topics in applied earth
691   observations and remote sensing 9, 1216–1228, 2015.
692 NASM: National Academies of Sciences, Engineering, and Medicine: Thriving on our changing plaent: A decadal strategy for
693   Earth observation from space. Washington, DC: The National Academies Press. doi: https://doi.org/10.17226/24938,
694   2018.
695 Niu, G., Yang, Z., Mitchell, K.E., Chen, F., Ek, M.B., Barlage, M., Kumar, A., Manning, K., Niyogi, D., Rosero, E., Tewari,
696   M., Xia, Y.: The community Noah land surface model with multiparameterization options (Noah-MP): 1. Model
697   description and evaluation with local-scale measurements. Journal of Geophysical Research: Atmospheres 116.
698   https://doi.org/10.1029/2010JD015139, 2011.
699 Niu, G.-Y., Yang, Z.-L.: Effects of vegetation canopy processes on snow surface energy and mass balances. Journal of
700   Geophysical Research: Atmospheres 109. https://doi.org/10.1029/2004JD004884, 2004.

701 Painter, T.H., Berisford, D.F., Boardman, J.W., Bormann, K.J., Deems, J.S., Gehrke, F., Hedrick, A., Joyce, M., Laidlaw, R.,
702   Marks, D., Mattmann, C., McGurk, B., Ramirez, P., Richardson, M., Skiles, S.M., Seidel, F.C., Winstral, A.: The
703   Airborne Snow Observatory: Fusion of scanning lidar, imaging spectrometer, and physically-based modeling for
704   mapping snow water equivalent and snow albedo. Remote Sensing of Environment 184, 139–152.
705   https://doi.org/10.1016/j.rse.2016.06.018, 2016.
706 Pflug, J.M., Hughes, M., Lundquist, J.D.: Downscaling snow deposition using historic snow depth patterns: Diagnosing
707   limitations from snowfall biases, winter snow losses, and interannual snow pattern repeatability. Water Resources
708   Research e2021WR029999. https://doi.org/10.1029/2021WR029999, 2021.
709 Pflug, J.M., Margulis, S.A., Lundquist, J.D.: Inferring watershed-scale mean snowfall magnitude and distribution using
710   multidecadal snow reanalysis patterns and snow pillow observations. Hydrological Processes 36, e14581, 2022.
711 Raleigh, M.S., Lundquist, J.D.: Comparing and combining SWE estimates from the SNOW-17 model using PRISM and SWE
712   reconstruction. Water Resources Research 48. https://doi.org/10.1029/2011WR010542, 2012.
713 Reichle, R.H., McLaughlin, D.B., Entekhabi, D.: Hydrologic Data Assimilation with the Ensemble Kalman Filter. Monthly
714   Weather Review 130, 103–114. https://doi.org/10.1175/1520-0493(2002)130<0103:HDAWTE>2.0.CO;2, 2002.
715 Rott, H., Yueh, S. H., Cline, D. W., Duguay, C., Essery, R., Haas, C., Hélière, F., Kern, M., Macelloni, G., Malnes, E.,
716   Thompson, A.: Cold regions hydrology high-resolution observatory for snow and cold land processes. Proceedings
717   of the IEEE, 98(5), 752-765, 2010.
718 Rott, H., Duguay, C., Etchevers, P., Essery, R., Hajnsek, I., Macelloni, G., Malnes, E., and Pulliainen, J.: CoReH2O Report
719   for mission selection: An Earth Explorer to observe snow and ice, Tech. rep., European Space Agency,
720   https://earth.esa.int/eogateway/documents/20142/37627/CoReH2O-Report-for-Mission-Selection-An-Earth-
721   Explorer-to-observe-snow-and-ice.pdf, 2012.
722 Ruiz, J.J., Lemmetyinen, J., Kontu, A., Tarvainen, R., Vehmas, R., Pulliainen, J., Praks, J.: Investigation of Environmental
723   Effects on Coherence Loss in SAR Interferometry for Snow Water Equivalent Retrieval. IEEE Transactions on
724   Geoscience and Remote Sensing 60, 1–15. https://doi.org/10.1109/TGRS.2022.3223760, 2022.
725 Schirmer, M., Wirz, V., Clifton, A., Lehning, M.: Persistence in intra-annual snow depth distribution: 1. Measurements and
726   topographic control: PERSISTENT SNOW DEPTH DEVELOPMENT, 1. Water Resources Research 47.
727   https://doi.org/10.1029/2010WR009426, 2011.
728 Singh, S., Durand, M., Kim, E., Barros, A.P: Bayesian physical-statistical retrieval of snow water equivalent and snow depth
729   from X- and Ku-band synthetic-aperture-radar demonstration using airborne SnowSAR in SnowEx17. EGUsphere 1
730   – 35. https://doi.org/10.5194/egusphere-2023-1987, 2023.
731 Sturm, M., Wagner, A.M.: Using repeated patterns in snow distribution modeling: An Arctic example. Water Resources
732   Research 46, 2010.
733 Terzago, S., Bongiovanni, G., von Hardenberg, J.: Seasonal forecasting of snow resources at Alpine sites. Hydrology and Earth
734   System Sciences 27, 519–542. https://doi.org/10.5194/hess-27-519-2023, 2023.
735 Trujillo, E., Ramírez, J.A., Elder, K.J.: Topographic, meteorologic, and canopy controls on the scaling characteristics of the
736   spatial distribution of snow depth fields. Water Resources Research 43, 2007.
737 Tsang, L., Durand, M., Derksen, C., Barros, A.P., Kang, D.-H., Lievens, H., Marshall, H.-P., Zhu, J., Johnson, J., King, J.,
738   Lemmetyinen, J., Sandells, M., Rutter, N., Siqueira, P., Nolin, A., Osmanoglu, B., Vuyovich, C., Kim, E., Taylor, D.,
739   Merkouriadi, I., Brucker, L., Navari, M., Dumont, M., Kelly, R., Kim, R.S., Liao, T.-H., Borah, F., Xu, X.: Review
740   article: Global monitoring of snow water equivalent using high-frequency radar remote sensing. The Cryosphere 16,
741   3531–3573. https://doi.org/10.5194/tc-16-3531-2022, 2022.
742 Wayand, N.E., Hamlet, A.F., Hughes, M., Feld, S.I., Lundquist, J.D.: Intercomparison of Meteorological Forcing Data from
743   Empirical and Mesoscale Model Sources in the North Fork American River Basin in Northern Sierra Nevada,
744   California. Journal of Hydrometeorology 14, 677–699. https://doi.org/10.1175/JHM-D-12-0102.1, 2013.
745 Woodruff, C.D., Qualls, R.J.: Recurrent Snowmelt Pattern Synthesis using Principal Component Analysis of Multi-Year
746   Remotely Sensed Snow Cover. Water Resources Research 55, 6869–6885. https://doi.org/10.1029/2018WR024546,
747   2019.
748 Wrzesien, M., Kumar, S.V., Vuyovich, C., Kim, R.S., Cho, E., Pflug, J.M., Konapala, G., Arsenault, K.R.: Merging remote
749   sensing and models to improve performance and accessibility of snow information, AGU Fall Meeting, Conference
750   on Hydrology, 2022.

751 Wrzesien, M.L., Kumar, S., Vuyovich, C., Gutmann, E.D., Kim, R.S., Forman, B.A., Durand, M., Raleigh, M.S., Webb, R.,
752   Houser, P.: Development of a "Nature Run" for Observing System Simulation Experiments (OSSEs) for Snow
753   Mission Development. Journal of Hydrometeorology 23, 351–375. https://doi.org/10.1175/JHM-D-21-0071.1, 2022.
754 Ying, Y.: Assimilating Observations with Spatially Correlated Errors Using a Serial Ensemble Filter with a Multiscale
755   Approach. Monthly Weather Review 148, 3397–3412. https://doi.org/10.1175/MWR-D-19-0387.1, 2020.
756 Yu, L., Fennel, K., Wang, B., Laurent, A., Thompson, K.R., Shay, L.K.: Evaluation of nonidentical versus identical twin
757   approaches for observation impact assessments: an ensemble-Kalman-filter-based ocean assimilation application for
758   the Gulf of Mexico. Ocean Science 15, 1801–1814. https://doi.org/10.5194/os-15-1801-2019, 2019.
759 Yueh, S. H., Dinardo, S. J., Akgiray, A., West, R., Cline, D. W., Elder, K.:. Airborne Ku-band polarimetric radar remote
760   sensing of terrestrial snow cover. IEEE Transactions on Geoscience and Remote Sensing, 47(10), 3347-3364. 2009.
761 Zhu, J., Tan, S., King, J., Derksen, C., Lemmetyinen, J., and Tsang, L.: Forward and inverse radar modeling of terrestrial snow
762   using SnowSAR Data, IEEE Transactions on Geoscience and Remote Sensing, 56(12), 7122-7132,
763   doi:10.1109/TGRS.2018.2848642, 2018.
764 Zhu, J., Tan, S., Tsang, L., Kang, D.K., and Kim, E.: Snow water equivalent retrieval using active and passive microwave
765   observations. Water Resources Research 57, no. 7, 2021.